Proceedings of ASME 2012 Fluids Engineering Division Summer Meeting
FEDSM2012
July 8-12, 2012, Rio Grande, Puerto Rico, USA

FEDSM2012-72378

MODELING AND SIMULATION OF MULTIPLE BUBBLE ENTRAINMENT AND INTERACTIONS WITH A TRAVELING VORTEX RING

Andrew J. Cihonski
Justin R. Finn
Sourabh V. Apte *
Computational Flow Physics Laboratory
Department of Mechanical, Industrial and Manufacturing Engineering
Oregon State University
Corvallis, Oregon 97331
Email: sva@engr.orst.edu

ABSTRACT

Bubble interactions with vortical structures are important to better understand the mechanisms of bubble induced boundary layer drag reduction and chemical mixing. Traditionally, many studies of disperse bubble or particle-laden flows have utilized an Euler-Lagrange two-way coupling approach, wherein the dispersed phase is assumed subgrid and its dynamics is modeled. In this work, results on full three-dimensional simulation of traveling vortex ring together with a few microbubbles are presented utilizing a volumetric coupling approach, wherein the displaced mass due to the presence of the bubbles is accounted for by using mixture theory based conservation laws in an Euler-Lagrange formulation. It is shown that the volumetric coupling approach is necessary to reproduce the experimental observations of Sridhar & Katz, JFM (1999). Experimental work by S&K on bubble entrainment into a traveling vortex ring has shown that the settling location of the bubble relative to the vortex core can be well predicted based on the ratio of the buoyancy force to the hydrodynamic pressure gradient. Additionally, the experimental results find that even at low volume fractions, bubble injection can significantly affect the structure of the vortex core. The two-way coupling model, wherein the fluid displacement due to bubble motion is neglected, of bubble-laden flows is unable to capture these effects on the vortical structure.

*Address all correspondence to this author.

NOMENCLATURE

- $\mathbf{u}_b$ bubble velocity.
- $\mathbf{u}_\ell$ liquid velocity.
- ρ_b bubble density.
- ρ_ℓ liquid density.
- d_b bubble diameter.
- θ_b bubble volume fraction.
- θ_ℓ liquid volume fraction.
- r_s bubble settling radius.
- θ_s bubble settling angle.
- C_D drag coefficient.
- C_L lift coefficient.
- C_{AM} added mass coefficient.
- Re_b Reynolds number of the bubble.
- St_b Stokes number.
- θ_e° azimuthal bubble position angle.
- t_{θ_e} bubble escape past θ_e°.
- Cr vortex core rise.
- E relative decay of angular momentum.
- W relative increase in peak vorticity.
- Γ_0 initial vortex circulation.

INTRODUCTION

The features of the interaction of vortical structures with bubbles are important to many applications, including bubble-

induced boundary layer drag reduction, chemical mixing in bubble column and stirred tank reactors as well as cavitating flows. Sridhar and Katz [1], hereafter referred to as S&K, showed that a few small Stokes number bubbles have the ability to augment the core structure of both laminar and turbulent traveling vortex rings during their entrainment cycle. Oweis et al. [2] studied the properties of bubble capture and cavitation in a line vortex. Their study utilized a one-way coupling approach to predict capture times, which was found to be accurate when utilized for small bubbles, but was not sufficient when bubble growth was a significant factor. [3], [4] and [5] utilized experimental methods to determine the appropriate choices for drag and lift coefficients on bubbles in vortical structures. Two-way coupling of bubble interactions with homogeneous isotropic turbulence was investigated by Mazzitelli et al. [6]. They concluded that bubble accumulation on the downward side of vortices was primarily due to the lift force, in what is known as the preferential sweeping mechanism.

Much of the computational work on bubble-laden turbulent flows at dilute to moderate volume loadings has utilized the point particle approach. Hsiao et al. [7] [8] used one-way coupling to study cavitation inception in a line vortex flow as well as tip vortex cavitation. Mattson and Mahesh [9] studied bubble transport using one-way coupling in boundary layer flows. Work by Shams et al. (2010) [10] has shown that in a rising bubble column, accounting for the mass displaced by the presence of bubbles and their motion (known as volumetric coupling) is required to properly simulate certain system properties. In addition, studies by Apte et al. (2008) [11] show the importance of these finite-size effects in gas-solid fluidized beds and slurry flows. Ferrante and Elghobashi [12] use this volumetric coupling approach with a two-fluid model to study the effects of microbubbles on Taylor-Green vortices. Their study finds an enhanced vortex decay rate dependent on bubble concentration as well as a positive correlation between enstrophy and flow divergence due to bubble accumulation in the core regions.

Research by Glezer (1988) [13] on the formation of vortex rings, found a suitable method for predicting vortex strength using a cylindrical slug model. Classification of laminar, transitional and turbulent vortex rings was also given based on the generator aspect ratio and the vortex ring strength. S&K, in follow-up work from their initial study, investigated the effects of bubbles on the structure of the vortex rings. It was concluded that at certain ratio of buoyancy to hydrodynamic pressure gradient forces the bubbles, even at extremely dilute volume loadings and a small (1/1000) density ratio, could significantly alter vortex structure [1]. Finn et al. [14] utilized volumetric coupling to study bubble entrainment in a traveling vortex tube, a two-dimensional approximation of the vortex ring case of S&K. Their work found that the inclusion of finite-size effects was necessary to reproduce the experimental observation of S&K for both bubble settling location as well as vortex core distortion. This motivates the current work on bubble entrainment in a three dimensional traveling vortex ring.

MATHEMATICAL FORMULATION

In this work, the liquid phase is handled in an Eulerian fashion using direct numerical simulation. Lagrangian tracking is utilized for bubble motion and coupled to the flow solver. Bubbles are assumed spherical and to be subgrid scale in size. Details of the numerical methodology can be found in Shams et al. [10] and Shams & Apte [15].

Continuous Phase

In the volumetric coupling formulation, the fluid phase equations are altered to account for the mass displaced by the presence and motion of the bubbles. Each bubble occupies a volume V_b, which corresponds to a local bubble volume fraction, θ_b. The local liquid volume fraction is defined as $\theta_\ell = 1 - \theta_b$. This formulation is consistent with the mixture theory approach of Joseph et al. [16, 17]. Equation 1 is the altered conservation of mass:

$$\frac{\partial}{\partial t}(\rho_\ell \theta_\ell) + \nabla \cdot (\rho_\ell \theta_\ell \mathbf{u}_\ell) = 0. \tag{1}$$

Note that in this form, the flow field, even for an incompressible fluid, is not divergence free. Rearrangement of Eqn. 1 yields an expression for the local divergence.

$$\nabla \cdot \mathbf{u}_\ell = -\frac{1}{\theta_\ell}\left(\frac{\partial \theta_\ell}{\partial t} - \mathbf{u}_\ell \cdot \nabla \theta_\ell\right). \tag{2}$$

In a similar manner, the conservation of momentum, Eqn. 3, is altered to include the presence of bubbles. The two-way momentum coupling source term is denoted by $\mathbf{f}_{b\to\ell}$.

$$\frac{\partial}{\partial t}(\rho_\ell \theta_\ell \mathbf{u}_\ell) + \nabla \cdot (\rho_\ell \theta_\ell \mathbf{u}_\ell \mathbf{u}_\ell) = -\theta_\ell \nabla P + \nabla \cdot (\theta_\ell \mu_\ell \mathbf{D}) - \theta_\ell \rho_\ell \mathbf{g} + \mathbf{f}_{b\to\ell} \tag{3}$$

where the deformation tensor is $\mathbf{D} = \nabla \mathbf{u}_\ell + \nabla \mathbf{u}_\ell^T$. The source term consists of the bubble surface forces and is handled as shown in Eqn. 4.

$$\mathbf{f}_{b\to\ell}(\mathbf{x}_{cv}) = -\sum_{b=1}^{N_b} \mathscr{G}_\Delta(\mathbf{x}_{cv}, \mathbf{x}_b)(\mathbf{F}_d + \mathbf{F}_\ell + \mathbf{F}_{am}) \tag{4}$$

here, $\mathscr{G}_\Delta$ denotes an interpolation function from the bubble locations on to the grid. Here x_{cv} and x_b are the centers of the control volume and bubble respectively. The total number of bubbles is N_b.

Dispersed Phase

The bubble phase is handled using the equations of motion developed by Maxey & Riley [18].

$$\frac{d}{dt}(\mathbf{x}_b) = \mathbf{u}_b \tag{5}$$

$$m_b \frac{d}{dt}(\mathbf{u}_b) = \sum \mathbf{F}_b. \tag{6}$$

Forces on bubbles are computed from explicit carrier phase information. The forces are used to update bubble velocity and position by solving the system of ordinary differential equations in Eqns. 5 and 6.

$$\sum \mathbf{F}_b = \mathbf{F}_g + \mathbf{F}_p + \mathbf{F}_d + \mathbf{F}_\ell + \mathbf{F}_{am}, \tag{7}$$

where x_b is the particle location, m_b is the mass of an individual particle, $\mathbf{u}_b$ is the particle velocity vector and $\mathbf{F}_b$ denotes a generic force acting on a particle. In this case $\mathbf{F}_b$ can be broken up into the pressure ($\mathbf{F}_p$), drag ($\mathbf{F}_g$), gravity ($\mathbf{F}_d$), lift ($\mathbf{F}_\ell$) and added mass ($\mathbf{F}_{am}$). In this formulation gravitational force is just the weight of the bubble:

$$\mathbf{F}_g = \rho_b V_b \mathbf{g}, \tag{8}$$

The volume of the individual particle is denoted as V_b, which is assumed to be perfectly spherical. The drag force on the particle is modeled using the standard drag equation for flow past a sphere:

$$\mathbf{F}_d = -(1/2) C_d \rho_\ell \pi r_b^2 |\mathbf{u}_b - \mathbf{u}_\ell| (\mathbf{u}_b - \mathbf{u}_\ell), \tag{9}$$

where C_d is the drag coefficient, and r_b is the particle radius. There are several models available to select from for the drag coefficient, each model has particular strengths. For the Reynolds number ranges and particle mass loadings being studied here, the Schiller and Nauman [19] drag curve has been selected. In this model the drag coefficient is modeled by Eqn. 10.

$$C_d = \frac{24}{Re_b}(1 + 0.15 Re_b^{0.687}), \tag{10}$$

in which Re_b is the particle Reynolds number, given by $Re_b = (\rho_b d_b |u_b - u_\ell|)/\mu_\ell$. The lift force is due to the relative velocity difference between the fluid and the particles, it results in lateral (around the cortex ring) particle motion. This is calculated as shown

$$\mathbf{F}_\ell = -C_\ell \rho_\ell \pi r_b^2 (\mathbf{u}_b - \mathbf{u}_\ell) \times (\nabla \times \mathbf{u}_\ell). \tag{11}$$

The coefficient of proportionality, C_ℓ, is estimated as $C_\ell = 0.59\alpha^{0.25}$ [5]. The added mass force ($\mathbf{F}_a$) comes from the amount of mass in addition to that naturally belonging to the particle which is displaced due to the bubbles motion. The added mass force is modeled as:

$$\mathbf{F}_{am} = -\frac{1}{2}\rho_\ell V_b \left(\frac{D\mathbf{u}_b}{Dt} - \frac{D\mathbf{u}_\ell}{Dt}\right). \tag{12}$$

The added mass force uses the standard added mass coefficient of $1/2$. The pressure force is that on particles due to the localized pressure gradients:

$$\mathbf{F}_p = -V_b \nabla p. \tag{13}$$

These forces comprise those taken into account through two-way coupling, i.e. the momentum transfer between the fluid and particles. Bubble-bubble collisions are neglected due to the extremely low volume fraction and bubbles are assumed to have a fixed size.

VORTEX RING SETUP

To create an appropriate vortex ring, a circular inlet with a radius of $0.05m$ is centered in a rectangular box with dimensions $0.8m \times 0.3m \times 0.3m$. The liquid density and viscosity are $\rho_\ell = 1000kg/m^3$ and $\nu_\ell = 1 \times 10^{-6} m^2/s$, respectively. The bubble density is $\rho_b = 1kg/m^3$. At $t = 0$ liquid is injected according to the velocity profile specified in Fig. 1.

This yields a traveling vortex ring that is self sustaining beyond the end of the computational domain. Iso-pressure contours are shown in Fig. 2 to visualize the propagation of the ring. All contours except the initial start up contour represent the same pressure level. The initial circulation estimate and the vortex Reynolds number are computed based on the work of Glezer [13]

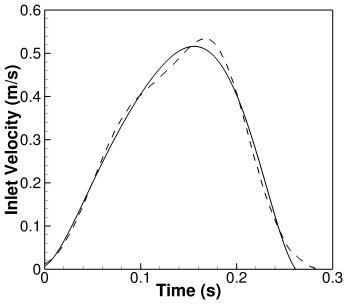

FIGURE 1. INLET VELOCITY PROFILE: (—) CURRENT WORK, (---) S&K EXPERIMENTAL PROFILE [1]

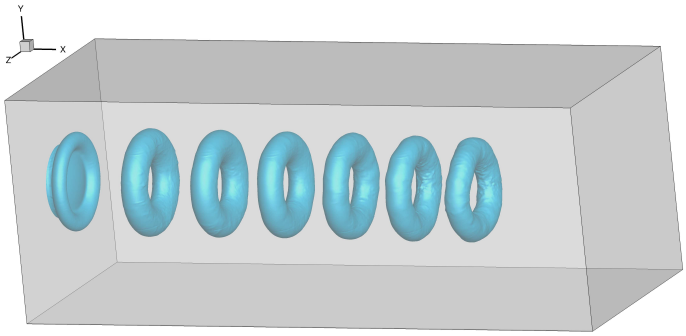

FIGURE 2. PROPAGATION OF A VORTEX RING WITHIN THE COMPUTATIONAL DOMAIN.

$$\Gamma_0 = \int_0^T \frac{u_0^2(t)}{2} dt = 0.0159;\ 0.0207;\ 0.0254\ m^2/s \quad (14)$$

$$Re_{vx} = \frac{1}{2\nu_\ell} \int_0^T u_0^2(t) dt = 15900;\ 20700;\ 25400 \quad (15)$$

to obtain the three different vortex strength used in this work. Scaling the inlet velocity profile achieves the changes in vortex strength desired.

The center of the vortex core (X_c, Y_c) is defined as the weighted center of vorticity, computed as shown in Eqn. 16, of a plane slice at the bottom of the vortex ring.

$$X_c = \sum_i X_i \omega_i^2 / \sum_i \omega_i^2 \quad ; \quad Y_c = \sum_i Y_i \omega_i^2 / \sum_i \omega_i^2 \quad (16)$$

In a perfectly symmetric vortex core on this slice, the center would be the point of zero velocity. In this work there is a slight streamwise elongation of the core as well as distortion effects, so these two points need not overlap. When the vortex center reaches $0.5m$ downstream from the inlet, a number of

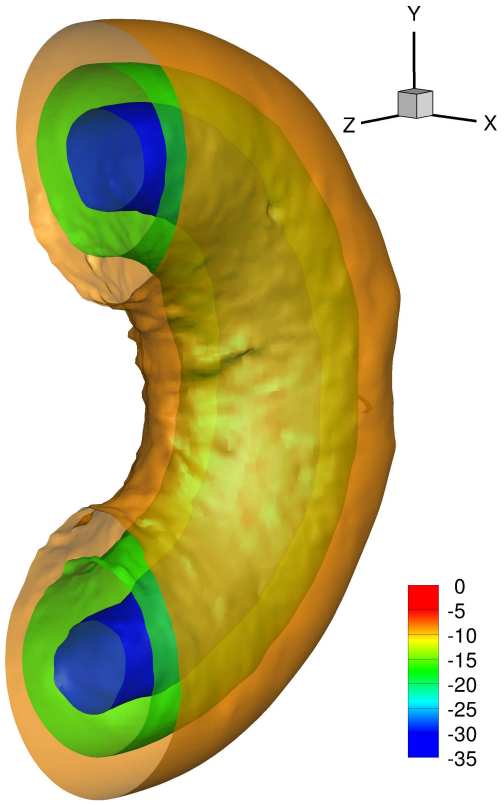

FIGURE 3. CONCENTRIC PRESSURE ISO-CONTOURS OF THE VORTEX RING: $\Gamma_0 = 0.0159\ m^2/s$

bubbles (N_b) are injected in front of and below the core center. At this point the vortex has well defined concentric strucutures of vorticity and pressure, see Fig. 3. As the vortex propagates downstream the bubbles entrain within the core. When the core center reaches $0.65m$ downstream from the inlet the simulation is stopped. This distance is far enough away from the outlet to avoid any spurious boundary effects. Parameters for the traveling vortex ring cases are shown in Tab. 1.

RESULTS

The effects of vortex entrainment on bubble motion as well as vortex distortion will be investigated in this section. To begin with, a discussion of the entrainment process and properties as well as some bubble escape observations will be presented. Then, the effect these bubbles have on vortex ring behavior will be presented.

Bubble Entrainment

As the released bubbles are entrained by the vortex they follow a spiraling path inward towards the center. Figure 4(a) shows

TABLE 1. VORTEX RING CASE STUDY PARAMETERS.

Case #	$\Gamma_0(m^2/s)$	$d_b(\mu m)$	St_b	N_b
1	0.0159	300	0.09	8
2	0.0159	500	0.27	8
3	0.0159	700	0.53	8
4	0.0159	900	0.87	8
5	0.0159	1100	1.30	8
6	0.0159	1300	1.81	8
7	0.0207	700	0.68	8
8	0.0254	500	0.43	8
9	0.0254	700	0.84	8
10	0.0254	900	1.39	8
11	0.0254	1100	2.07	8
12	0.0254	1300	2.89	8

three sample bubble trajectories for cases 1, 3 and 5 each utilizing the volumetric coupling approach. The larger the bubble the sharper the spiral towards the center of the vortex ring. Although this only provides one sample bubble from each of the three cases, it is easy to visualize the difference in settling location, the location where the bubble stays at equilibrium, for the three different bubble sizes. It is also possible to see the effect of the changing Stokes number on the entrainment process. The volatility in the paths taken by the three bubbles is clearly dependent on size (Stokes number). The predictive path differences between one-way, two-way and volumetric coupling are shown in figure 4(b). The bubble motion computed using one-way and two-way coupling are negligibly different, suggesting that the two-way coupling momentum source term is quite small compared to the vortex's momentum.

Not all bubbles entrain to a settling location and stay there. As Fig. 5 shows, depending on the case, bubbles paths can vary greatly in relation to the core. S&K developed a relationship to estimate the settling location of a bubble relative to the core center. They used dimensional analysis to show that the settling location is a strong function of the ratio of the buoyancy force to the hydrodynamic pressure gradient, $r/R = f(gd_b^3/\Gamma_0^2)$. In other words, for the purposes of this study, the smaller the bubble and/or stronger the vortex, the closer to the core center the bubble will settle. Figure 5(a) shows the path traversed by a $500\mu m$ bubble in a strong vortex (Case #8). Note that all eight bubbles stay relatively close together and do not veer to either side of the

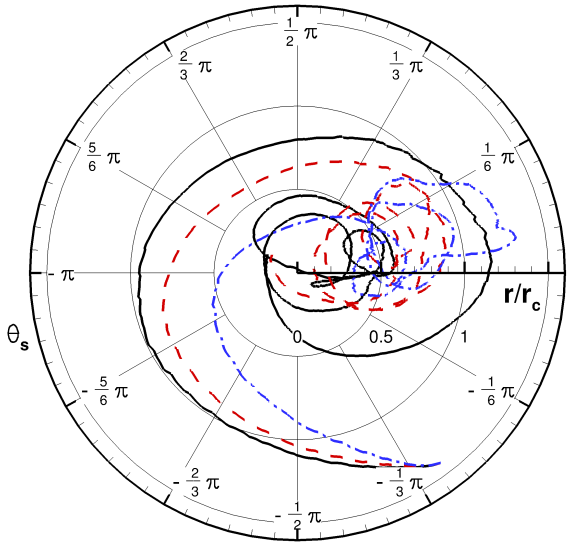

(a) $\Gamma_0 = 0.0159\ m^2/s$: (—) $300\mu m$, (---) $700\mu m$, (-·-·) $1100\mu m$

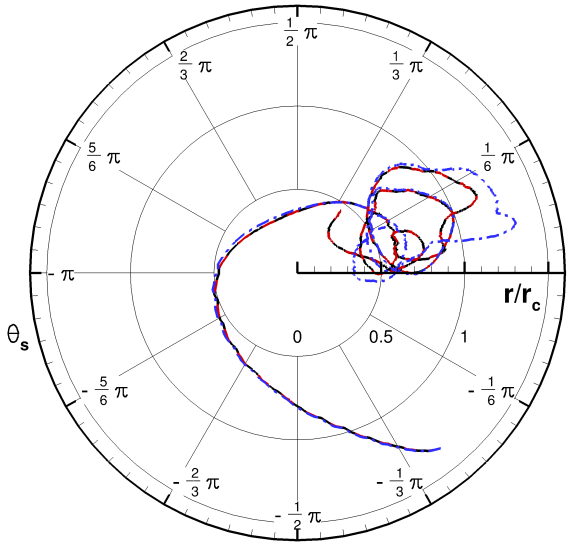

(b) $\Gamma_0 = 0.0159\ m^2/s$, $d_b = 1100\mu m$: (—) One-Way, (---) Two-Way, (-·-·) Volumetric

FIGURE 4. BUBBLE TRAJECTORIES RELATIVE TO THE VORTEX CORE CENTER

vortex ring. In contrast, Figs. 5(b) and 5(c) show moderate and significant bubble escape (bubble motion along the core up the side of the vortex), respectively.

Table 2 gives measurements for the percentage of simulation time, $t_\theta\%$, that the bubbles are contained within θ degrees azimuthally of the plane of injection (i.e. the bottom slice of the vortex core). In the strong vortex cases bubble escape is not sig-

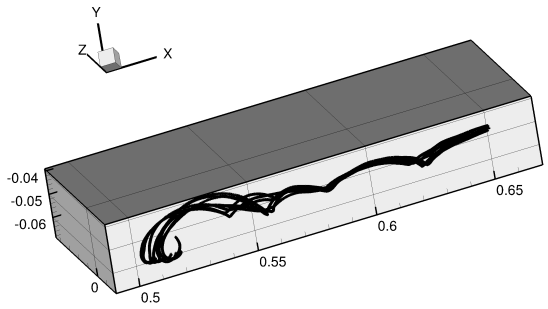

(a) $\Gamma_0 = 0.0254\ m^2/s$, $d_b = 500\mu m$ (Case #8)

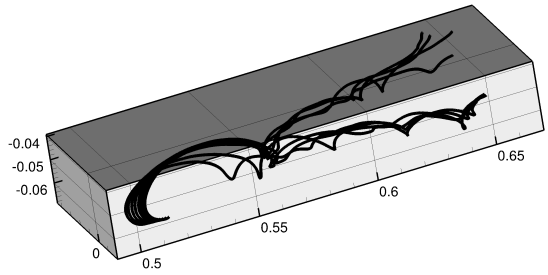

(b) $\Gamma_0 = 0.0159\ m^2/s$: $d_b = 700\mu m$ (Case #3)

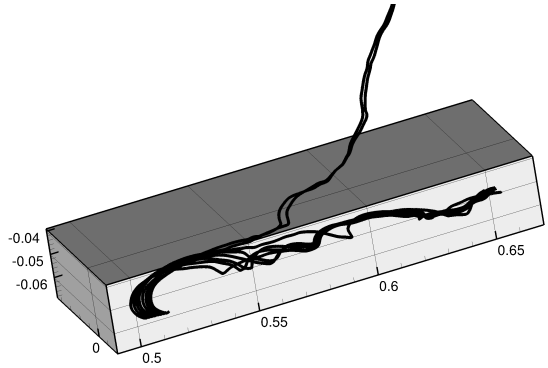

(c) $\Gamma_0 = 0.0159\ m^2/s$ $d_b = 1100\mu m$ (Case #5)

FIGURE 5. EXAMPLES OF PATHS TRAVERSED BY BUBBLES WITHIN VORTEX RING: (a) NEGLIGIBLE BUBBLE ESCAPE, (b) MODERATE BUBBLE ESCAPE, (c) SIGNIFICANT BUBBLE ESCAPE.

TABLE 2. BUBBLE ESCAPE MEASUREMENTS.

Case #	$t_{5.1}(\%)$	$t_{10.2}(\%)$	$t_{20.4}(\%)$
1	50.9	71.3	86.4
2	34.1	51.7	75.3
3	39.9	53.0	80.3
4	29.3	42.6	76.6
5	30.3	42.9	84.4
6	29.8	38.5	92.5
7	41.3	84.1	100.0
8	49.7	100.0	100.0
9	49.6	100.0	100.0
10	62.7	100.0	100.0
11	48.5	100.0	100.0
12	51.9	100.0	100.0

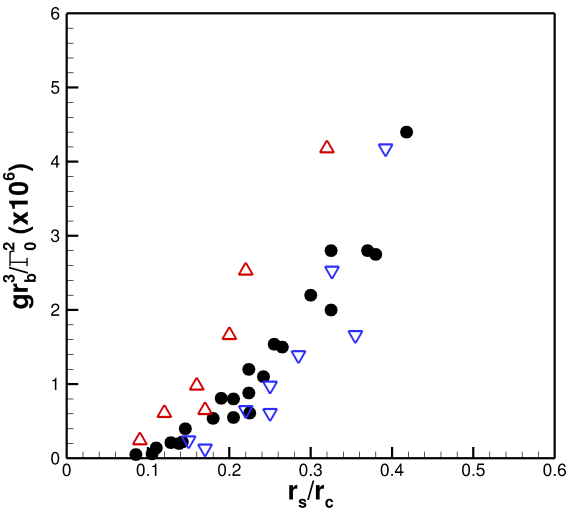

FIGURE 6. SETTLING LOCATION: (•) EXPERIMENTAL, (Δ) TWO-WAY COUPLING, (∇) VOLUMETRIC COUPLING

nificant, but still can occur to a small degree. Note that in many cases, bubbles stay within 10° of the injection plane for the entire simulation. While the pattern does not perfectly hold, it would seem that the settling parameter developed by S&K, gd_b^3/Γ_0^2, is also predictive of bubble escape properties. All measurements in Tab. 2 are based on volumetric coupling. While some escape occurs with one-way and two-way coupling it is significantly less than is present in volumetric coupling.

Settling location measurements were made by averaging the position of the bubbles relative to the vortex core after the initial bubble entrainment was done and before escape became significant, they are plotted alongside the experimental data of S&K in

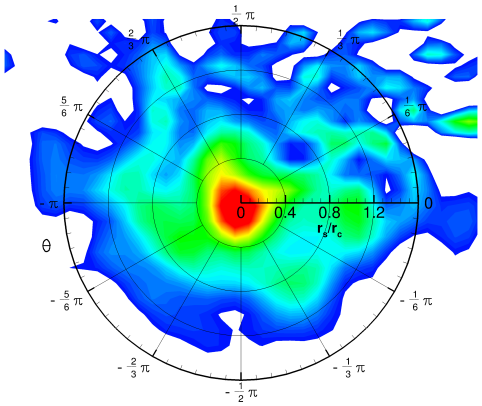

FIGURE 7. (a) VORTICITY CONTOURS AT THE TIME OF BUBBLE INJECTION ($X_c = 0.5m$), $\Gamma_0 = 0.0159m^2/s$.

Fig. 6. Settling did not occur in any reasonable sense for cases 5 and 6, the measurement for case 4 is also a bit tenuous due to the short settling time. The one-way and two-way coupling approaches under predict the settling location of the bubbles. These methods were relatively accurate for small bubbles where vortex distortion is small, but performed poorly for larger Stokes number bubbles. It would seem that accounting for finite-size effects is necessary, as the settling location matches the experimental data of S&K quite well, unlike the two-way coupling approach results. This shows that the vortex distortion effects caused by displacing the fluid mass at bubble locations is an important factor in this process.

Vortex Ring Alteration

The primary result of the work of S&K [1] was that even at very dilute loading, a small number of low Stokes number bubbles can dramatically alter the structure of a vortex ring. This section will discuss some of the effects of bubble entrainment on the vortex ring.

Figure 7 shows a cross section of a bubble-free vortex ring, note the roughly concentric contours of vorticity. Figures 8(a) - 8(c) show how the initial vortex is distorted in three different cases. While the clean gas contours provide one distinct continuous region of high vorticity, the others have a high vorticity region, as well as other regions of near max vorticity throughout, as well as regions of extremely low vorticity near the vortex center. This is a good visual measure of vortex distortion.

A core center increase in vorticity as well as an increase in peak vorticity due to bubble entrainment were both found by S&K and Finn et al. [1,14]. Figure 9(a) shows a proportional rise is core center mean vorticity as a function of bubble Stokes number. Note that the profiles for bubble sizes $d_b = 700$ and $900\mu m$ do not fit the trend, which suggests bubble escape is also a factor in this feature. This is conceptually in line with the results of

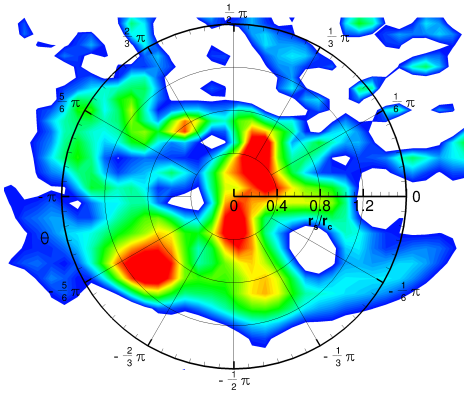

(a) Case # 1

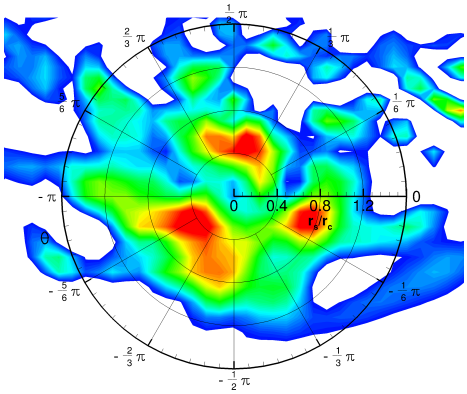

(b) Case # 3

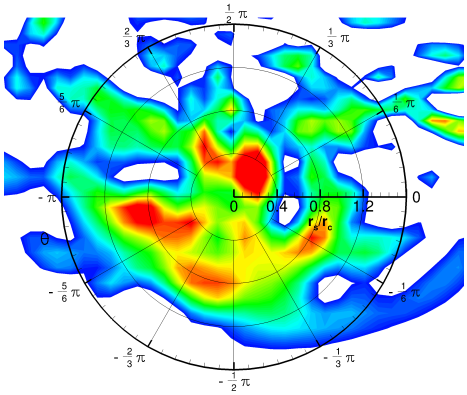

(c) Case # 5

FIGURE 8. VORTICITY CONTOURS AT THE PLANE OF BUBBLE INJECTION AFTER BUBBLE ENTRAINMENT ($X_c = 0.65m$).

S&K [1], who obtained maximum vortex distortion for $700\mu m$ bubbles. Finn et al. [14] saw a clear trend purely in relation to bubble size within a given vortex strength. This is likely due to the two-dimensionality of the work, causing bubble escape to not be a significant factor. This is only found to occur in significant

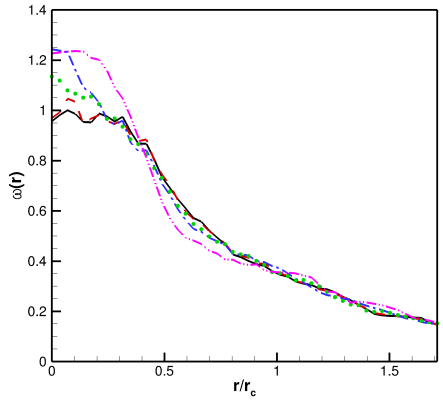

(a) $\Gamma_0 = 0.0159\ m^2/s$: (—) Clean Gas, (---) $500\mu m$, (-·-·) $700\mu m$, (●●●) $900\mu m$, (-·····) $1100\mu m$

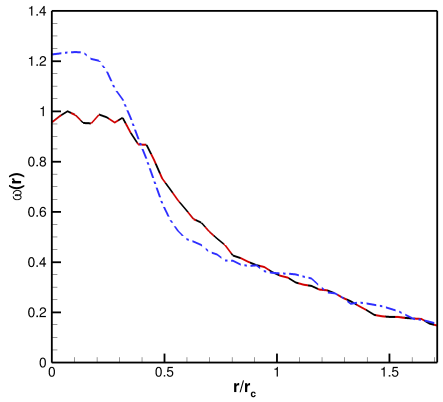

(b) $\Gamma_0 = 0.0159\ m^2/s$, $d_b = 1100\mu m$: (—) One-Way, (---) Two-Way, (-·-·) Volumetric

FIGURE 9. RADIALLY AVERAGED VORTICITY PROFILES ($X_c = 0.65m$).

portions when utilizing volumetric coupling. Two-way coupling measurements differ from clean gas measurements by less than 1%, see Fig. 9(b). The two-way coupling momentum source due to bubble motion relative to liquid motion was an insignificant contribution to the total momentum.

Several measures of vortex distortion are considered here. First is the relative decay rate of angular momentum, E, computed by taking the mean angular momentum loss rate, $\varepsilon = \frac{d(L_{vx})}{dt}$, where $L_{vx} = \sum_{core\ cv} \rho_\ell u_\theta r_{cv} V_{cv}$. W is the relative increase in peak vorticity, calculated as

$$E = \frac{\overline{\hat{\varepsilon} - \varepsilon}}{\varepsilon} \times 100 \quad ; \quad W = \frac{\overline{\hat{\omega}_p - \omega_p}}{\omega_p} \times 100 \qquad (17)$$

TABLE 3. VORTEX DISTORTION MEASUREMENTS.

Case #	$E(\%)$	$W(\%)$	$I_{0.4}(m^2/s)$	$I(m^2/s)$	$Cr(x10^{-5}m)$
1	0.93	11.2	0.1	0.2	2.15
2	2.57	11.6	0.3	0.6	8.85
3	1.59	10.0	1.9	2.9	5.15
4	1.52	3.9	1.1	1.8	10.65
5	1.34	6.5	3.3	5.5	46.15
6	2.40	3.6	2.7	4.4	53.15
7	2.36	2.1	1.0	2.1	7.2
8	2.80	-0.1	0.2	0.3	7.5
9	4.45	-0.1	0.4	0.8	3.75
10	7.48	0.1	1.0	2.2	22.9
11	7.65	2.1	1.2	2.4	20.9
12	10.00	4.3	1.4	2.5	33.6

where ˆ denotes the volumetric coupling case measurement and no superscript indicates the bubble-free vortex. Another measure of distortion taken is the integrated difference in the absolute value of vorticity between the volumetric coupling cases and clean gas case, as in Eqn. 18. $I_{0.4}$ and I are taken to show the difference in the vortex distortion near the core center and away from the center. $I_{0.4}$ denotes the radial integrated difference for $0 \leq r/r_c \leq 0.4$.

$$I_{0.4} = \int_0^{0.4r_c} |\hat{\omega} - \omega| dr \quad ; \quad I = \int_0^{1.71r_c} |\hat{\omega} - \omega| dr \qquad (18)$$

S&K [1] used the peak increase in vorticity in combination with the induced core rise of the flow (Cr) to classify distortion. Table 3 gives values of each of these measurements by case.

The general trend of increasing distortive properties with increasing bubble Stokes number is clear. This trend is very strong for cases 8-12, where $\Gamma_0 = 0.254 m^2/s$, due to bubble escape being fairly minimal in comparison with the weaker vortex cases. By entraining the bubble for an extended period of time near the core center the effect is not diluted out over a larger volume or slice of the vortex ring. Using viscous diffusion as an estimate for how far the effect of bubbles can propagate away from their bodies, S&K estimated the distance as about 1 bubble diameter laterally [1]. Thus the effect is concentrated in the region of measurement. In cases 1-6 there are two competing effects, a larger

reaction force caused by larger Stokes number bubbles, as well as the decreased time this reaction force is applied to the plane of bubble injection due to escape. The core rise measurements are in qualitative agreement with those of S&K, however their study found larger maximum core rise and found it to be better correlated to vortex fragmentation than was seen in the current work [1].

Figure 6 was not just useful for classifying bubble settling locations relative to the core, but also to classify vortex distortion. S&K observed similar properties of distortion as this study, where bubble escape seems to limit deformation due to bubble presence. This is due to vortex reparation mechanisms which cause the distorted vortex, once the bubbles have escaped the plane of bubble injection, to repair itself to a similar profile as before bubble injection [1]. This makes quantitatively analyzing the effects of bubble entrainment difficult, as deformation can be repaired in a relatively quick manner. Finn et al. [14] did not observe these trends since bubble escape was negligible in the two-dimensional vortex tube case, thus a direct correlation between Stokes number and distortion was found. S&K found that vortex distortion was not present in cases where the bubble settling close to the core, $r_s/r_c < 0.13$, as well as for bubbles that settled far from the core, or did not settle at all, $r_s/r_c > 0.45$. Marginal distortion was found for $0.14 < r_s/r_c < 0.2$ and $0.4 < r_s/r_c < 0.45$, with a mix of severe and marginal distortion between those ranges [1]. This result is in general agreement with the observations in this work. The smallest bubbles do not exhibit enough force to distort, the largest do not settle long enough to cause a larger contribution by some measures. Bubble escape properties are intimately related to the lateral (azimuthal direction) pressure gradient generated by vortex distortion. This increased core pressure causes bubbles to settle further out, and be more likely to escape along the contour of largest pressure gradient, which is along the center of the vortex core out of the plane of injection. Thus, gd_b^3/Γ_0^2 is also an excellent indicator of vortex distortive properties.

CONCLUSIONS

Direct numerical simulation of a traveling vortex ring was performed using Lagrangian particle tracking. The effectiveness of the point particle method and the volumetric coupling method are analyzed and compared to the experimental results of Sridhar and Katz [1] and the two-dimensional simulations of Finn et al. [14]. It was found that accounting for the mass displaced caused by the presence of bubbles is necessary to adequately reproduce experimental observation of bubble settling and escape as well as vortex distortion properties. Bubble behavior was analyzed by studying escape characteristics as well as settling properties of various Stokes number bubbles. The lift coefficient of S&K [5] was utilized and, in combination with volumetric coupling, results in agreement with experimental observations and data on bubble escape and settling, as well as the results of Finn et al. [14]. Vortex distortion was classified using several methods including the radially averaged mean vorticity profile, peak vorticity, angular momentum decay, core-assymetry and fragmentation. Two-way coupling calculations showed minimal vortex distortion by any measure. The dimensionless parameter gd_b^3/Γ_0^2 was confirmed to be an excellent indicator of all three properties (settling, escape, distortion). Further work on the mechanisms and strength of vortex reparation effects would be a beneficial extension of this work.

ACKNOWLEDGMENT

This work is supported by Department of Energy's National Energy Technology Laboratory through the URS contract number 41817M4077 and monitored by Dr. Cathy Summers. Computing time on TACC's Lonestar machine is highly appreciated.

REFERENCES

[1] Sridhar, G., and Katz, J., 1999. "Effect of entrained bubbles on the structure of vortex rings". *Journal of Fluid Mechanics,* ***397***, pp. 171–202.

[2] Oweis, G. F., van der Hout, I. E., Iyer, C., Tryggvason, G., and Ceccio, S. L., 2005. "Capture and inception of bubbles near line vortices". *Physics of Fluids,* ***17***(2), p. 022105.

[3] Van Nierop, E. A., Luther, S., Bluemink, J. J., Magnaudet, J., Prosperetti, A., and Lohse, D., 2007. "Drag and lift forces on bubbles in a rotating flow". *Journal of Fluid Mechanics,* ***571***, Jan., p. 439.

[4] Bluemink, J. J., Lohse, D., Prosperetti, A., and Van Wijngaarden, L., 2009. "Drag and lift forces on particles in a rotating flow". *Journal of Fluid Mechanics,* ***643***, Dec., p. 1.

[5] Sridhar, G., and Katz, J., 1995. "Drag and lift forces on microscopic bubbles entrained by a vortex". *Physics of Fluids,* ***7***(2), p. 389.

[6] Mazzitelli, I. M., Lohse, D., and Toschi, F., 2003. "The effect of microbubbles on developed turbulence". *Physics of Fluids,* ***15***(1), p. L5.

[7] Hsiao, C., Chahine, G. L., and Liu, H., 2003. "Scaling effect on prediction of cavitation inception in a line vortex flow". *Journal of Fluids Engineering,* ***125***(1), p. 53.

[8] Hsiao, C., and Chahine, G., 2004. "Prediction of tip vortex cavitation inception using coupled spherical and nonspherical bubble models and Navier?Stokes computations". *Journal of Marine Science and Technology,* ***8***(3), Jan., pp. 99–108.

[9] Mattson, M., and Mahesh, K., 2011. "Simulation of bubble migration in a turbulent boundary layer". *Physics of Fluids,* ***23***(4), p. 045107.

[10] Shams, E., Finn, J., and Apte, S. V., 2011. "A numerical scheme for Euler-Lagrange simulation of bubbly flows in complex systems". *International Journal for Numerical Methods in Fluids,* ***67***(12), Dec., pp. 1865–1898.

[11] Apte, S., Mahesh, K., and Lundgren, T., 2008. "Accounting for finite-size effects in simulations of disperse particle-laden flows". *International Journal of Multiphase Flow,* ***34***(3), Mar., pp. 260–271.

[12] Ferrante, A., and Elghobashi, S. E., 2007. "On the effects of microbubbles on TaylorGreen vortex flow". *Journal of Fluid Mechanics,* ***572***, Jan., p. 145.

[13] Glezer, A., 1988. "The formation of vortex rings". *Physics of Fluids,* ***31***(12), p. 3532.

[14] Finn, J., Shams, E., and Apte, S. V., 2011. "Modeling and simulation of multiple bubble entrainment and interactions with two dimensional vortical flows". *Physics of Fluids,* ***23***(2), p. 023301.

[15] Shams, E., and Apte, S. V., 2010. "Prediction of Small-Scale cavitation in a high speed flow over an open cavity using Large-Eddy simulation". *Journal of Fluids Engineering,* ***132***(11), p. 111301.

[16] Joseph, D., Lundgren, T., Jackson, R., and Saville, D., 1990. "Ensemble averaged and mixture theory equations for incompressible fluidparticle suspensions". *International Journal of Multiphase Flow,* ***16***(1), Jan., pp. 35–42.

[17] Prosperetti, A., and Zhang, D. Z., 1995. "Finite-particle-size effects in disperse two-phase flows". *Theoretical and Computational Fluid Dynamics,* ***7***(6), Nov., pp. 429–440.

[18] Maxey, M. R., 1983. "Equation of motion for a small rigid sphere in a nonuniform flow". *Physics of Fluids,* ***26***(4), p. 883.

[19] Schiller, L., and Naumann, A., 1935. "A drag coefficient correlation". *VDI Z.,* ***77***(318).